A CASE STUDY ON THE USE OF DIFFERENTIAL SAR TOMOGRAPHY FOR MEASURING DEFORMATION IN LAYOVER AREAS IN RUGGED ALPINE TERRAIN

Muhammad A. Siddique[1], *Irena Hajnsek*[1,3], *Othmar Frey*[1,2]

[1]Earth Observation and Remote Sensing, ETH Zurich, Switzerland
[2]Gamma Remote Sensing AG, Gümligen, Switzerland
[3]Microwaves and Radar Institute, German Aerospace Center - DLR, Oberpfaffenhofen, Germany

ABSTRACT

Differential SAR tomography is a means to resolve layover of temporally coherent scatterers while simultaneously estimating their elevation and average deformation. In alpine regions, drastic height variations result in frequent layovers which are rejected during typical persistent scatterer interferometric (PSI) analyses. In this paper, we explore the potential of tomographic techniques to improve deformation sampling in an alpine region of interest relative to a PSI-based deformation assessment. The mitigation of the atmospheric phase contributions, as required for both tomography and PSI, is often more involved in alpine regions due to strong spatial variations of the local atmospheric conditions and propagation paths through the troposphere. We assume a linear multivariate dependence of atmospheric phase on the spatial location and height of the scatterers, estimate it using universal/regression kriging and subsequently incorporate it within the tomographic focusing. Experiments are performed on an interferometric stack comprising of 32 Cosmo-SkyMed strimap images acquired in the summers of 2008-2013 over Mattervalley in the Swiss Alps.

***Index Terms*—** SAR tomography, persistent scatterer interferometry, multi-baseline interferometry, Cosmo-SkyMed

1. INTRODUCTION

Persistent scatterer interferometry (PSI) [1, 2] is an operational SAR-based method to measure surface deformation in the wake of human activity or prior to natural mass movements. The observed scene should have a sufficient number of targets that exhibit temporally coherent and point-like backscattering, which are the defining features of a persistent scatterer (PS). Since PSI conventionally builds upon a single scatterer phase model, any multiplicity of PS in the same resolution cell, as for the case of a layover, is rejected. In general, there is a low prevalence of PS candidates in suburban or natural terrains such as the alps and the adjoining valleys. At the same time, layovers are more often owing to drastic height variations across the scene. Provided the fact that often mass movements of interest occur in mountainous areas, it may happen that a given region of interest (RoI) for the measurements falls in a layover. The aforementioned limitations motivate us to explore methods to address layovers in alpine terrain and measure deformation for any stable scatterers in layover. In this context, we look forward to the use of differential SAR tomography [3].

This research project has been funded by the Swiss Space Office, State Secretariat for Education and Research of the Swiss Confederation (SER/SSO), via the MdP2012 initiative. The DEM used in this work is ©swisstopo. T. Strozzi from GAMMA Remote Sensing is acknowledged for providing a PSI solution of the region.

Differential SAR tomography has thus far been applied for deformation monitoring in urban regions or specific infrastructure [4, 5, 6]. Prior to tomographic inversion, the interferometric stack needs to be phase calibrated by compensating for the atmosphere-induced phase delays. The relatively wider prevalence of PS candidates in urban scenes facilitates estimation of the atmospheric phase screen (APS). Contrarily, the estimation in alpine regions is more involved. Firstly, there may be a lack of sufficient PS candidates close to the RoI to allow for a reasonable estimation and subsequent extrapolation over the RoI. Secondly, due to the extremely rugged topography which can change by as much as a few kilometers between the valley floor and the mountain top, the local atmospheric conditions and the propagation paths through the troposphere may strongly vary spatially. Keeping in consideration the aforementioned challenges, we conduct a case study to investigate the applicability and usefulness of differential SAR tomography for improving deformation sampling in alpine terrain relative to a PSI-based assessment.

2. METHODS

2.1. Persistent scatterer interferometry (PSI)

The Interferometric Point Target Analysis [2, 7] toolbox is used to perform a PSI analysis. An iterative regression-based strategy is implemented to identify a set of persistent scatterers (PS) exhibiting good quality (in terms of low residual phase variance). The PSI solution obtained after several iterations comprises the estimated residual topography, the average deformation velocity and the atmosphere-induced phase delays for each PS. A linear model of the atmospheric phases with respect to height was used to model possible vertical stratification in the atmosphere [8].

2.2. Differential SAR tomography

Considering a given range-azimuth pixel (r, a), a mathematical model for differential SAR tomography [3, 9, 10, 5] is as follows:

$$y_n^{(\mathrm{r},\mathrm{a})} = \int_{\mathbb{P}} \alpha\left(\mathbf{p}\right) \exp\left[-j\varphi_n\left(\mathbf{p}\right)\right] \mathrm{d}\mathbf{p} \tag{1}$$

where $y_n^{(\mathrm{r},\mathrm{a})}$ is the single-look complex (SLC) pixel value in n^{th} layer of the coregistered stack, $n = 0, 1, \ldots N-1$ and $\alpha\left(\mathbf{p}\right)$ is the target reflectivity profile as a function of the parameter vector $\mathbf{p} = [s, v]$, where s is the unknown scatterer elevation along the perpendicular to the line of sight (LOS) axis, and v is the average deformation velocity in the LOS. Assuming the stack is phase calibrated, the interferometric phase, $\varphi_n\left(\mathbf{p}\right)$ is modeled as

$$\varphi_n\left(\mathbf{p}\right) = 2k\left[\triangle r_n\left(s\right) + vt_n\right] \tag{2}$$

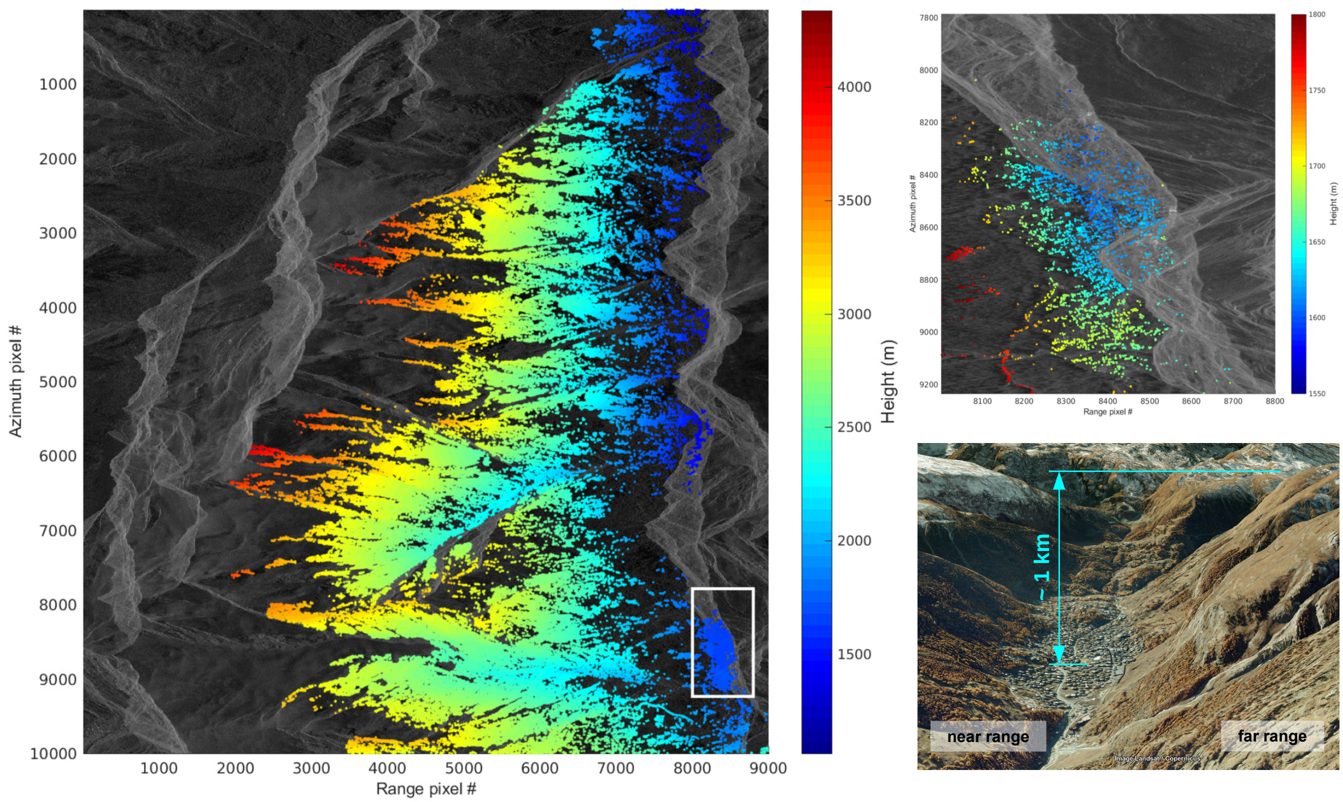

Fig. 1. *Left*: Cosmo-SkyMed SAR intensity image of the Mattervalley in Swiss Alps. The colored dots represent the persistent scatterers identified in the scene with an iterative PSI approach. *Right top*: The region of interest (RoI) for tomographic inversion, highlighted in white colored rectangle in the full scene. Layover of the alp (in far range) on the valley floor is clearly visible. *Right bottom*: Google Earth image of the RoI i.e., Zermatt valley, dated August 30, 2009.

where t_n is the temporal baseline for the n^{th} layer, and $\triangle r_n(s)$ is the geometrical sensor-to-target path-length difference [10, 5]. $\mathbb{P}$ represents the parameter space.

2.3. Regression kriging of atmospheric phases

Differential SAR tomography has thus far been applied for local infrastructure in urban areas where the underlying topography is generally flat. It is assumed that the atmosphere is exhibiting spatially low-frequency behavior and any topography-dependent variation is negligible. Within this context, the unwrapped atmospheric phases computed for the PS during the prior PSI processing can be spatially filtered in local neighborhood and extrapolated over the scene to estimate an APS for each layer in the stack (as in our earlier works [5, 11, 12]). However, in the case of alpine regions, the drastic variations in topography incur two critical implications for tomography. Firstly, a height-dependent phase delay variation owing to vertical stratification of the atmosphere cannot be ignored. Secondly, depending on the acquisition geometry, the possibly large height difference among the scatterers in layover implies that the spatial location of the individual scatterers in map coordinates (after geocoding) can also be very different. Therefore, the atmospheric correction needed for one scatterer may be very different from the other, notwithstanding that they are in the same range-azimuth pixel. Hence, a single correction for a range-azimuth pixel would likely not suffice. Instead, the atmospheric phases have to be estimated and compensated for within the tomographic focusing at each point of interest along the elevation axis. With these concerns, we model the unwrapped atmospheric phases $\mathcal{A}_n$ for the n^{th} layer, with a multivariate linear regression as follows:

$$\mathcal{A}_n(x) = \beta_n^0 + \beta_n^1 x_e + \beta_n^2 x_n + \beta_n^3 x_h + \varepsilon(x) \tag{3}$$

$$= \mathbf{x}^T \boldsymbol{\beta}_n + \varepsilon(x) \tag{4}$$

where $x = \{x_e, x_n, x_h\}$ represents a general 3D location in terms of easting (x_e), northing (x_n) and height (x_h), $x = \mathbb{T}\{\mathrm{r}, \mathrm{a}, s\}$ where $\mathbb{T}$ is the geocoding transformation operator, and β terms are the regression coefficients. The residue $\varepsilon(x)$ is assumed to be a zero-mean, spatially correlated second-order stationary random process. It implies that its spatial correlation depends on the lag, l between two locations. Further assuming *isotropy* (direction independence of the semivariance of ε), we consider that the spatial correlation depends only on the magnitude of the lag itself, which corresponds to Euclidean distance between two locations in map geometry in our case. Using the atmospheric phases of the PS estimated in the prior PSI processing, and their map coordinates as spatial regressors, we obtain sample variogram for each interferometric layer as follows:

$$\hat{\gamma}_n(l) = \frac{1}{2N_{\text{ps}}} \sum_{i=1}^{N_{\text{ps}}} \left(\hat{\varepsilon}_n(x_i) - \hat{\varepsilon}_n(x_i + l)\right)^2 \tag{5}$$

where N_{ps} refers to the number of the PS used in the computation. The PS exhibiting significant deformation are ignored [13]. The sample variogram for each layer is then 'best' fit with a *non-negative*

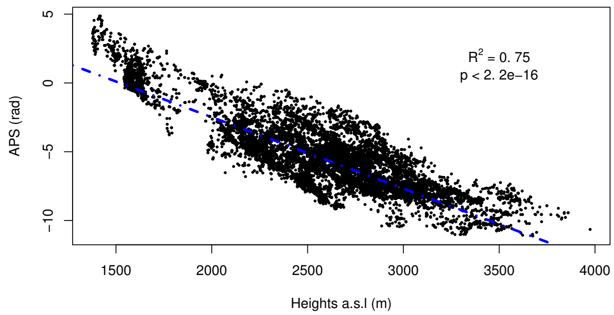

Fig. 2. Scatter plot of the unwrapped atmospheric phases against topography for the PS identified over the entire scene shown in Fig. 1 (left), for an example interferometric layer from the stack. The dotted line represents a univariate linear regression fit.

definite model (among a family of variogram models) to avoid singularity in kriging equations. The universal/regression kriging-based best linear unbiased predictor of the atmospheric phase at a location x_0 is then computed as follows:

$$\hat{\mathcal{A}}_n(x_0) = \mathbf{x}_0^T \hat{\boldsymbol{\beta}}_n + \boldsymbol{\omega}\left(\mathbf{A}_n - \mathbf{X}\hat{\boldsymbol{\beta}}_n\right) \tag{6}$$

where $\mathbf{A}_n = \left[\mathcal{A}_n(x_1), \mathcal{A}_n(x_2), \dots, \mathcal{A}_n(x_{N_{\mathrm{ps}}})\right]^T$, $\mathbf{X}$ is the design matrix comprising of the spatial regressors (map coordinates of the PS) and $\boldsymbol{\omega}$ is the vector of *simple kriging* weights [14]. The regression coefficients can be estimated with generalized least squares: $\hat{\boldsymbol{\beta}}_n = \left(\mathbf{X}^T\mathbf{V}^{-1}\mathbf{X}\right)^{-1}\mathbf{X}\mathbf{V}^{-1}\mathbf{A}_n$, where $\mathbf{V}$ is the covariance matrix of the atmospheric phases $\mathbf{A}_n$ [14].

2.4. Tomographic inversion

The 2D reflectivity profile for a range-azimuth pixel (r, a) with SLC vector $\mathbf{y}$ is retrieved with beamforming (BF) as follows:

$$\hat{\alpha}(s, v) = \frac{1}{N}\left[e^{-j\vartheta_0(s,v)}, e^{-j\vartheta_1(s,v)}, \dots, e^{-j\vartheta_{N-1}(s,v)}\right]^* \mathbf{y} \tag{7}$$

where $\vartheta_n(s, v) = \varphi_n(s, v) + \hat{\mathcal{A}}_n(\mathbb{T}\{\mathrm{r}, \mathrm{a}, s\})$. For the estimation of the unknown scatterer elevation and deformation, and single and double scatterer detection, we apply BF-based maximizations under the *sequential generalized likelihood ratio test with cancellation* (SGLRTC) scheme [9, 5].

3. DATA & REGION OF INTEREST (ROI)

The data used in this work is an interferometric stack comprising of 32 Cosmo-SkyMed stripmap images acquired over the Mattervalley in Swiss Alps in the summers between 2008-2013. The region is known to have many active landslides, rockslides and rockfalls, as highlighted in an earlier work [7]. The RoI selected for tomographic analysis is the Zermatt valley, as shown in Fig. 1 (right). The SAR image clearly shows the layover cast over the valley floor. The optical image from Google Earth shows a 3D perspective of the area. The height difference between the valley floor and the mountain top is on the order of a kilometer. We can see vegetation stretched over the slopes in near range. As to the one in far range, which casts the layover, we can observe some bare rocks on the mountainside which may exhibit coherent scattering over long term. It is the layover of scatterers with point-like characteristics that we look forward to resolving with differential tomography, within the valley

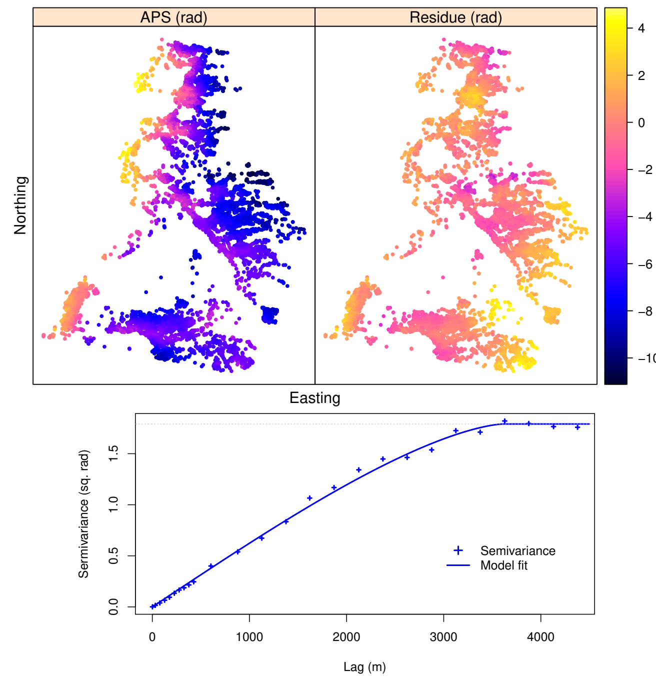

Fig. 3. *Top-left*: Geocoded unwrapped atmospheric phases for the PS identified over the entire scene, for an example layer from the interferometric stack. *Top-right*: Residue of multivariate linear regression of the atmospheric phases against spatial coordinates and height. *Bottom*: Sample variogram and model fit (circular).

(between man-made infrastructure) as well as between the valley and the mountainside (if any).

4. RESULTS

Fig. 1 shows the PS identified in an IPTA-based PSI analysis. A scatter plot of the unwrapped atmospheric phases of the PS is shown against their heights in Fig. 2 for an example interferometric layer from the stack. In Fig. 3, these atmospheric phases and the residue after a multivariate regression against height and spatial coordinates are shown in map geometry. Fig. 4 shows the single and double scatterers obtained using a BF-based differential tomographic inversion with detection thresholds set at 0.48 (referred to [5, 9] for details).

5. DISCUSSION & OUTLOOK

The distribution of the PS identified over the full scene with a PSI analysis is shown in Fig. 1 (left). The PS are color-coded with the retrieved heights, which span roughly between 1200 - 4000 m a.s.l., corresponding mostly to bare rocks in layover-free areas. These phases are shown in a scatter plot against the heights in Fig. 2 for an example interferometric layer from the stack. A regression fit against the heights is also plotted; it shows a significant linear dependence indicating possible vertical stratification of the atmospheric phase delay differences between the example and the reference layer in the stack. In Fig. 3 (top right), the residue after a multivariate regression fit of the phases against height and spatial map coordinates (easting, northing) is shown. The spatial trends are statistically significant, and the residue shows a smooth behavior indicating spatial correlation. The sample variogram in Fig. 3 (bottom) shows the de-

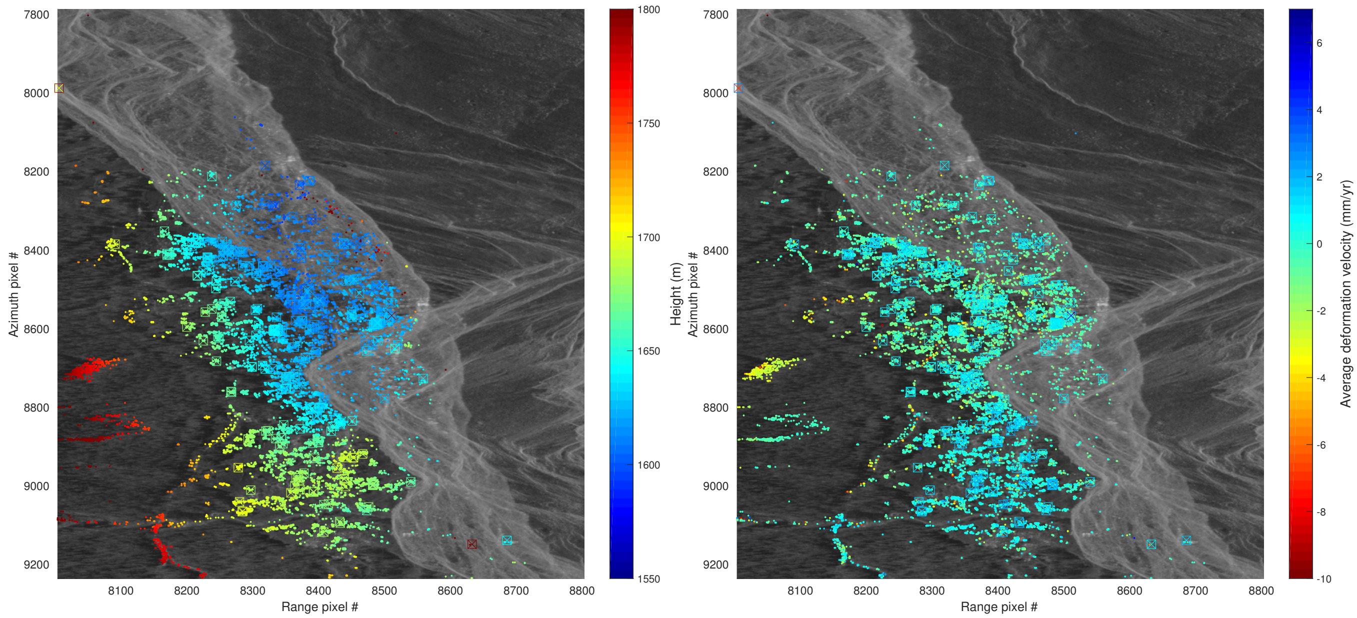

Fig. 4. Single and double scatterers obtained with differential SAR tomographic inversion, under the SGLRTC detection strategy with detection thresholds set at 0.48 (referred to [5, 9] for details). Single scatterers are marked with '·'. The first and the second in case of a double scatterer are marked with '□' and '×', respectively. The size of the markers for double scatterers is exaggerated for better readability. *Left*: Estimated height a.s.l. in m. *Right*: Estimated average deformation velocity in mm/yr.

cline in spatial correlation as the lag increases. Multivariate regression fitting and variogram modeling is performed for all the layers in the stack. The spatial and height-dependent trends are more pronounced in some layers than in the others. In each case, a regression kriging-based estimate of the atmosphere at any 3D location in map geometry (where we intend to retrieve target reflectivity with tomographic inversion) exploits the estimated trends and the statistics of the residue. Fig. 4 shows the distribution of the single and double scatterers obtained in the RoI with BF-based tomographic inversion. Although we observe more single scatterers compared to the PS solution, the apparent gain in deformation sampling remains to be assessed vis-à-vis quality of the scatterers [11]. A few single scatterers are detected on the mountainside around 230 m above the valley floor where no PS were found with the PSI processing. It substantiates the usefulness of the kriging-based atmospheric estimations introduced in the paper. However, the applicability of tomographic inversion for this RoI remains limited as only 274 double scatterers have been detected, and nearly all of them belong to the layovers occurring in the built-up area in the valley floor.

6. REFERENCES

[1] A. Ferretti, C. Prati, and F. Rocca, "Permanent scatterers in SAR interferometry," *IEEE Trans. on Geosc. and Remote Sens.*, vol. 39, no. 1, pp. 8–20, 2001.

[2] C. Werner, U. Wegmüller, T. Strozzi, and A. Wiesmann, "Interferometric point target analysis for deformation mapping," in *Proc. IEEE Int. Geosci. Remote Sens. Symp.*, 2003, pp. 4362–4364.

[3] F. Lombardini, "Differential tomography: A new framework for SAR interferometry," *IEEE Trans. Geosci. Remote Sens.*, vol. 43, no. 1, pp. 37–44, 2005.

[4] X. Zhu and R. Bamler, "Superresolving SAR tomography for multidimensional imaging of urban areas: Compressive sensing-based TomoSAR inversion," *IEEE Signal Process. Mag.*, vol. 31, no. 4, pp. 51–58, 2014.

[5] M. Siddique, U. Wegmuller, I. Hajnsek, and O. Frey, "Single-look SAR tomography as an add-on to PSI for improved deformation analysis in urban areas," *IEEE Trans. Geosci. Remote Sens.*, vol. 54, no. 10, pp. 6119–6137, Oct 2016.

[6] D. Reale, G. Fornaro, and A. Pauciullo, "Extension of 4-D SAR imaging to the monitoring of thermally dilating scatterers," *IEEE Trans. Geosci. Remote Sens.*, vol. 51, no. 12, pp. 5296–5306, 2013.

[7] T. Strozzi, H. Raetzo, U. Wegmuller, J. Papke, R. Caduff, C. Werner, and A. Wiesmann, *Satellite and terrestrial radar interferometry for the measurement of slope deformation*, pp. 161–165, Springer International Publishing, Cham, 2015.

[8] T. Strozzi, R. Caduff, U Wegmller, H. Raetzo, and M. Hauser, "Widespread surface subsidence measured with satellite SAR interferometry in the Swiss alpine range associated with the construction of the Gotthard Base Tunnel," *Remote Sens. of Environm.*, vol. 190, pp. 1 – 12, 2017.

[9] A. Pauciullo, D. Reale, A. De Maio, and G. Fornaro, "Detection of double scatterers in SAR tomography," *IEEE Trans. Geosci. Remote Sens.*, vol. 50, no. 9, pp. 3567–3586, 2012.

[10] G. Fornaro, A. Pauciullo, D. Reale, and S. Verde, "Multilook SAR tomography for 3D reconstruction and monitoring of single structures applied to Cosmo-SkyMed data," *IEEE J. Sel. Topics Appl. Earth Observ. Remote Sens.*, vol. 7, no. 7, pp. 2776–2785, July 2014.

[11] M. Siddique, U. Wegmuller, I. Hajnsek, and O. Frey, "Sar tomography as an add-on to PSI: Gain in deformation sampling vis-a-vis quality of the detected scatterers," in *Proc. IEEE Int. Geosci. Remote Sens. Symp.*, July 2016, pp. 1452–1455.

[12] O. Frey, M. Siddique, I. Hajnsek, U. Wegmüller, and C. Werner, "Combining SAR tomography and a PSI approach for high-resolution 3-D imaging of an urban area," in *Proc. 10th European Conf. on SAR*, 2014, pp. 1045–1048.

[13] D. Bekaert, A. Hooper, and T. Wright, "A spatially variable power law tropospheric correction technique for InSAR data," *Jour. Geophys. Res.: Solid Earth*, vol. 120, no. 2, pp. 1345–1356, 2015.

[14] R. Bivand, E. Pebesma, and V. Gmez-Rubio, *Applied Spatial Data Analysis with R*, Springer-Verlag New York, 2008.